where F and G are sums of products of three and four variables respectively, with all variables to the power one. The products of three variables are of the form XYY, while there are no two terms that contain the same combination of Y's, and those of four variables are of the form $XXYY$ or $YYYY$. Let us consider the integration with respect to Y_1. Denote by $Y_1 f$ the terms in F depending on Y_1 and by $Y_1 g$ the terms in G depending on Y_1. The integration with respect to Y_1 gives

$$\int_{-\infty}^{\infty} \exp\left[-Y_1^2+2N^{-1/2}Y_1(f-N^{-1/2}g)\right]\mathrm{d}Y_1 = \pi^{1/2}\exp\left(N^{-1}f^2\right)\left[1+O(N^{-3/2})\right]. \quad (16)$$

The terms in f^2 can be divided into two groups: (*a*) terms of the form $XXYY$ depending on two different Y's; these terms are of the same class as the remaining terms of G; (*b*) terms of the form X^2Y^2; these terms are independent of the signs of the X's and are neglected [they belong to the same class as the terms of order N^{-1} not depending on the phases, which have been neglected in (14)]. Continuing in this way for the other integrations it is seen that $P_1(X_1,X_2,X_3,X_4,X_{12},X_{23},X_{31})$ is obtained from (15) by leaving out the terms depending on the Y's and by multiplying by $\pi^{7/2}$. Next, employing (4) and replacing N by $N/2$ we obtain

$$\begin{aligned}
&P_{\bar{1}}(S_1,S_2,S_3,S_4,S_{12},S_{23},S_{31})\\
&=(2\pi)^{-7/2}\exp\left[-\tfrac{1}{2}(S_1^2+S_2^2+S_3^2+S_4^2+S_{12}^2+S_{23}^2+S_{31}^2)\right.\\
&+N^{-1/2}(S_1S_2S_{12}+S_3S_4S_{12}+S_2S_3S_{23}\\
&+S_1S_4S_{23}+S_1S_3S_{31}+S_2S_4S_{31})\\
&-N^{-1}(S_1S_3S_{12}S_{23}+S_2S_4S_{12}S_{23}\\
&+S_1S_2S_{23}S_{31}+S_3S_4S_{23}S_{31}+S_2S_3S_{31}S_{12}\\
&\left.+S_1S_4S_{31}S_{12}+2S_1S_2S_3S_4)\right], \quad (17)
\end{aligned}$$

which is correct up to and including those terms of order N^{-1} that depend on the signs of the S's. This formula is identical with the one derived by Green & Hauptman (1976).

Concluding remarks

A general procedure has been given to obtain joint probability distributions of structure factors for structures in $P\bar{1}$ from those for structures in $P1$. Some examples, of increasing complexity, have been given. It is stressed that this procedure leads to $P\bar{1}$ distributions with the same probabilistic background as the $P1$ distributions from which they are derived.

The idea of considering a $P\bar{1}$ structure as the sum of two $P1$ structures which led to the procedure described in this paper was suggested by Dr J. Kroon. The author thanks Drs J. Kroon and H. Krabbendam and Professor A. F. Peerdeman for stimulating discussions and critical reading of the manuscript.

References

COCHRAN, W. & WOOLFSON, M. M. (1955). *Acta Cryst.* **8**, 1–12.
GIACOVAZZO, C. (1975). *Acta Cryst.* A**31**, 252–259.
GIACOVAZZO, C. (1976). *Acta Cryst.* A**32**, 91–99.
GIACOVAZZO, C. (1977). *Acta Cryst.* A**33**, 50–54.
GREEN, E. A. & HAUPTMAN, H. (1976). *Acta Cryst.* A**32**, 43–45.
HAUPTMAN, H. (1975). *Acta Cryst.* A**31**, 671–679.
HEINERMAN, J. J. L. (1977*a*). *Acta Cryst.* A**33**, 100–106.
HEINERMAN, J. J. L. (1977*b*). Submitted to *Acta Cryst.* A, but see footnote to Giacovazzo (1977).
WILSON, A. J. C. (1949). *Acta Cryst.* **2**, 318–321.

Acta Cryst. (1977). A**33**, 109–113

Approximations for the Calculation of High-Resolution Electron-Microscope Images of Thin Films

BY P. L. FEJES*

Department of Physics, Arizona State University, Tempe, Arizona 85281, *USA*

(*Received* 13 *February* 1976; *accepted* 25 *July* 1976)

Phase-grating calculations were carried out to calculate lattice images from thin crystals. A method for including the effect of chromatic aberration in these calculations is shown and the results are compared with experimental images. The improved agreement of calculations with experiment when chromatic aberration is taken into account is shown.

Introduction

By high-resolution electron microscopy it is possible to observe images of crystal structures with a resolution of about 3 Å. This type of imaging is being carried out in the study of a number of compounds having large unit cells such that features inside the unit cells can easily be identified. Complex oxide structures as well as many mineral structures have been studied. For a review of this work see for example Allpress & Sanders (1973), Buseck & Iijima (1974) and Cowley & Iijima (1976).

* Present address: Fritz-Haber-Institut der Max-Planck-Gesellschaft, 1 Berlin 33, Faradayweg 4–6, Germany (BRD).

A very useful feature of these high-resolution images is found in that when they are taken under certain well defined conditions, which are easily attainable experimentally, they represent closely a projection, along the incident beam direction, of the crystal potential. Images with this property will be referred to here as good images.

A set of imaging conditions which have been found to give good images is listed below.

(1) An incident electron energy of 100 keV was used.

(2) The crystal was lined up with one of the densely occupied atomic-row directions parallel to the incident beam direction to an accuracy of $\sim 2 \times 10^{-3}$ rad of arc.

(3) An objective aperture was used that transmitted diffracted beams up to a maximum scattering angle given by $2(\sin\theta)/\lambda = 0{\cdot}33$ Å^{-1}.

(4) The spherical aberration constant of the microscope was estimated to be 1·8 mm (from the manufacturer's data).

(5) The objective lens was underfocused by an estimated 600 to 1000 Å from the Gaussian focus plane.

(6) The beam divergence of the incident beam had a half angle of $1{\cdot}4 \times 10^{-3}$ rad of arc.

(7) The crystal thickness was estimated to be less than about 100 Å. The images were taken from wedge-shaped crystals and the regions giving good images range from the thin edge up to a point where the thickness is estimated to be approximately 100 Å. The image detail seems to be unchanged in this range but the high-resolution detail changes greatly for larger crystal thickness.

These are the conditions (with the exception of the fifth one) under which the experimental images shown below were all taken, and it is these conditions which the image calculations should attempt to approximate.

Weak-phase objects

The weak-phase object approximation (WPOA) can be used to predict the image contrast when the total phase change due to the object is small. For a discussion of this, see for instance Cowley & Iijima (1972). In this approximation, the image contrast (under the above imaging conditions) is directly proportional to the projected crystal potential:

$$I(\mathbf{r}) \simeq 1 - 2\sigma\varphi(\mathbf{r}) \qquad (1)$$

where $\varphi(\mathbf{r})$ is the potential distribution projected along the incident beam direction and $\sigma = \pi/\lambda V$ is the interaction constant, V being the energy and λ the wavelength of the incident electrons.

However, the WPOA is only valid when, for the maximum phase change due to the object, $\sigma\varphi(\mathbf{r}) \ll 1$. This means that for substances such as $Ti_2Nb_{10}O_{29}$, the WPOA is only valid for crystal thicknesses of less than ~ 6 Å, while good images are obtained from much thicker crystals under conditions similar to those indicated for the WPOA.

Strong phase objects

Imaging from a phase object (weak or strong) at small defocus can be treated in terms of the charge-density approximation as has been done by Lynch, Moodie & O'Keefe (1975). However, here we shall only suggest an intuitive argument to show why the WPOA could predict the correct experimental conditions for obtaining a good image from a crystal that is definitely not a weak-phase object.

Consider a peak in the projected crystal potential $\varphi(\mathbf{r})$ due to a row of atoms in the direction of the incident beam. This is from a strong-phase object and so the maximum value of $\sigma\varphi(\mathbf{r})$ is greater than $\pi/2$ as is drawn in Fig. 1(*a*). The transmission function, assuming a purely phase object, is

$$q(\mathbf{r}) = \exp\left[-i\sigma\varphi(\mathbf{r})\right]. \qquad (2)$$

The real and imaginary parts of $q(\mathbf{r})$ are shown in Fig. 1(*b*) and (*c*). They oscillate rapidly near the peak in the projected potential.

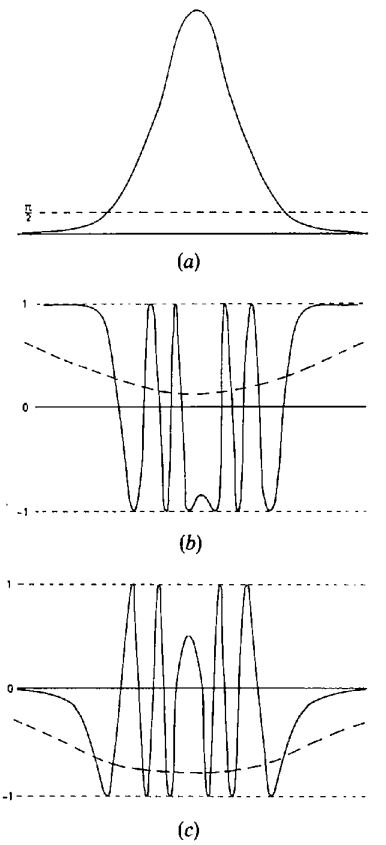

Fig. 1. (*a*) The phase change $\sigma\varphi(\mathbf{r})$ due to a row of atoms along the incident beam direction. (*b*) The solid line represents the real part of the transmission function due to this row of atoms and the dashed line represents the result expected when this function is convoluted with the aperture function. (*c*) The solid line represents the imaginary part of the transmission function due to the row of atoms and the dashed line represents the result when this function is convoluted with the aperture function.

Now an aperture is introduced into the back-focal plane of the objective lens. The wave function in the image plane then becomes

$$\psi(\mathbf{r}) = \exp\left[-i\sigma\varphi(\mathbf{r})\right] * \mathscr{F}A(\mathbf{u}) \qquad (3)$$

where $A(\mathbf{u})$ is the transmission function of the objective aperture with $\mathbf{u}$ being a vector in reciprocal space. The symbol $*$ represents a convolution integral and $\mathscr{F}$ represents a Fourier transform.

If the width of the original peak in the projected potential is about 0·5 Å and the aperture size limits the resolution to about 3 Å, then this will have the effect of smearing out the oscillations in the real and imaginary parts of $q(\mathbf{r})$ as is shown by the dashed lines in Fig. 1(*b*) and (*c*). Near the centre of the peak in the projected potential, the real part of $\psi(\mathbf{r})$ will be near zero and also the imaginary part will be small because the convolution in (3) represents an averaging over many rapid oscillations. If the function $\psi(\mathbf{r})$ were such that $|\psi(\mathbf{r})|^2 = 1$, then it could be represented by

$$\psi(\mathbf{r}) = \exp\left[-i\sigma\varphi'(\mathbf{r})\right]$$

where $\varphi'(\mathbf{r})$ is an effective potential which peaks at the positions of the atom rows. The broken curves in Fig. 1(*b*) and (*c*) indicate that because of the smearing of the oscillations in $q(\mathbf{r})$, $\sigma\varphi'(\mathbf{r})$ has a maximum value less than $\pi/2$ and so φ' represents the projected potential from a weak-phase object.

Near the position of the peak in the projected potential $|\psi(\mathbf{r})|^2 < 1$ because both the real and imaginary parts are small. Therefore the wave function, as modified by the objective aperture, can be described by

$$\psi(\mathbf{r}) = \exp\left[-i\sigma\varphi'(\mathbf{r}) - \mu'(\mathbf{r})\right] \qquad (4)$$

where $\mu'(\mathbf{r})$ is an effective absorption due to the effect of the objective aperture. It peaks at the positions of the centres of the atom rows and increases with thickness.

Equation (4) describes the transmission function of a crystal which acts as a weak-phase object together with an absorption potential peaked at the atom positions. Thus the image from a strong-phase object can be approximated as the image from a weak-phase object with absorption; so that WPOA arguments concerning imaging conditions should hold so long as the transmission function of the crystal can be given by (2).

It should be noted that the above argument is in no way rigorous and does not predict that the WPOA should give correct quantitative predictions of contrast in images from a strong-phase object. For instance, the WPOA predicts that the contrast in the image from a crystal is linear with crystal thickness [equation (5)]. However, *n*-beam dynamical calculations show that this is not so (Fejes, 1972), as is expected since $\varphi'(\mathbf{r})$ and $\mu'(\mathbf{r})$ are both highly non-linear with crystal thickness.

WPOA considerations can therefore be used for a qualitative description of images but for a proper calculation of images, dynamical calculations are necessary, such as phase-grating calculations as are done below.

Calculation of images

For the calculation of high-resolution images that can be compared with experiment, it is important that the effects of the electron microscope parameters on the imaging process should be well understood. Phase-grating calculations (Cowley & Moodie, 1960) were carried out for crystals of 10 Å thickness, using (3) to find the wave function, and the results were compared with experimental through-focus series of images taken by S. Iijima. For the complete through-focus series, the details of the experimental images did not change (except possibly for the overall contrast) with crystal thickness over a large range, and so no attempt has been made to determine the exact crystal thickness for these comparisons. The defocus steps were known from a calibration of the objective-lens control of the JEM 100B microscope and the absolute defocus values were obtained by comparing the experimental and calculated images.

The initial calculations included only the effects of defocus, spherical aberration and the objective aperture. The images calculated for a through-focus series from $Ti_2Nb_{10}O_{29}$, assuming a structure determined by Wadsley (1961), are compared with an experimental series from the same substance in Fig. 2(*a*). The calculations assume a spherical aberration constant of 1·8 mm and a maximum spatial frequency transmitted by the aperture of 0·33 $Å^{-1}$.

Even though the calculations were done with parameters approximating to the experimental conditions as closely as possible, the calculated images are seen to contain much more detail than the experimental ones and the agreement with the observed high-resolution detail is poor. This can be understood if one considers the WPOA which imposes the condition for good imaging that $\sin\chi(\mathbf{u}) \simeq -1$ for all values of spatial frequencies important in the imaging. $\chi(\mathbf{u})$ is the phase change due to defocus and spherical aberration and is given by

$$\chi(\mathbf{u}) = \pi\lambda\varepsilon u^2 + \tfrac{1}{2}\pi\lambda^3 C_s u^4 \qquad (5)$$

where the spatial frequency $|\mathbf{u}|$ has the value $2(\sin\theta)/\lambda$. Fig. 3 shows $\sin\chi(\mathbf{u})$ drawn for a defocus of -800 Å which is the value at which a good image is obtained experimentally. This shows that for spatial frequencies between 0·26 and 0·3 $Å^{-1}$, $\sin\chi(\mathbf{u})$ has the wrong sign and so these spatial frequencies will be imaged with reverse contrast, giving the false high-resolution detail in the image. The experimental images do not show such fine detail, suggesting that these spatial frequencies are absent in the images.

The images were recalculated using an objective aperture that removes spatial frequencies higher than 0·263 $Å^{-1}$. This time, the agreement with experiment (Fig. 2*b*) was much better. However, the parameters

used in the calculation do not agree with the experimental parameters. This problem can be overcome by the inclusion of chromatic aberration in the calculations.

Derivation of the effect of chromatic aberration

Chromatic aberration is produced by the spread in focal length of the objective lens due to a spread in energies of the electrons being imaged, and to instabilities in the objective lens. The effect on the image due to this spread in the focal length can be calculated in the following way.

The image at a particular value of defocus ε is given by

$$I_\varepsilon(\mathbf{r})=\psi_\varepsilon(\mathbf{r})\psi_\varepsilon^*(\mathbf{r}) \tag{6}$$

where $\psi_\varepsilon(\mathbf{r})$ is the wave amplitude on a plane distance ε from the exit surface of the crystal. From Fresnel diffraction, we have

$$\psi_\varepsilon(\mathbf{r})=\psi_0(\mathbf{r})*\frac{i}{\lambda\varepsilon}\exp\left(-\frac{i\pi r^2}{\lambda\varepsilon}\right). \tag{7}$$

Fourier transforming (6) gives

$$\begin{aligned}\mathscr{I}_\varepsilon(\mathbf{u})&=\Psi_\varepsilon(\mathbf{u})*\Psi_\varepsilon^*(-\mathbf{u})\\&=\int\int\Psi_\varepsilon(\mathbf{u}')\Psi_\varepsilon^*(\mathbf{u}'-\mathbf{u})\mathrm{d}^2\mathbf{u}'\end{aligned} \tag{8}$$

where $\Psi_\varepsilon(\mathbf{u})=\mathscr{F}\psi_\varepsilon(\mathbf{r})$, and Fourier transforming (7) gives

$$\Psi_\varepsilon(\mathbf{u})=\Psi_0(\mathbf{u})\exp(i\pi\lambda\varepsilon u^2). \tag{9}$$

To include chromatic aberration, the intensity must be averaged over defocus so that

$$I(\mathbf{r})=\int_{-\infty}^{\infty}I_\varepsilon(\mathbf{r})D(\varepsilon)\mathrm{d}\varepsilon \tag{10}$$

or, Fourier transforming (10),

$$\mathscr{I}(\mathbf{u})=\int_{-\infty}^{\infty}\mathscr{I}_\varepsilon(\mathbf{u})D(\varepsilon)\mathrm{d}\varepsilon. \tag{11}$$

Substituting (8) and (9) into (11) and changing the order of integration,

$$\begin{aligned}\mathscr{I}(\mathbf{u})=&\int\int\Psi_0(\mathbf{u}')\Psi_0^*(\mathbf{u}'-\mathbf{u})\\&\times\left(\int_{-\infty}^{\infty}D(\varepsilon)\exp\{i\pi\lambda\varepsilon[u'^2-(\mathbf{u}'-\mathbf{u})^2]\}\mathrm{d}\varepsilon\right)\mathrm{d}^2\mathbf{u}'.\end{aligned} \tag{12}$$

Approximating the defocus distribution $D(\varepsilon)$ by a Gaussian with a standard deviation Δ about a mean value ε_0 gives

$$D(\varepsilon)=\frac{1}{\Delta\sqrt{2\pi}}\exp\left[-\frac{(\varepsilon-\varepsilon_0)^2}{2\Delta^2}\right] \tag{13}$$

and substituting into (12) gives

$$\begin{aligned}\mathscr{I}(\mathbf{u})=&\int\int{}^{\Delta}\Psi(\mathbf{u}'){}^{\Delta}\Psi^*(\mathbf{u}'-\mathbf{u})\\&\times\exp[\pi^2\lambda^2\Delta^2u'^2(\mathbf{u}'-\mathbf{u})^2]\mathrm{d}^2\mathbf{u}'\end{aligned} \tag{14a}$$

where

$${}^{\Delta}\Psi(\mathbf{u})=\Psi_{\varepsilon_0}(\mathbf{u})\exp(-\tfrac{1}{2}\pi^2\lambda^2\Delta^2u^4). \tag{14b}$$

The intensity distribution in the image is then given by

$$I(\mathbf{r})=\mathscr{F}.\mathscr{I}(\mathbf{u}). \tag{15}$$

$\mathscr{I}(\mathbf{u})$ can easily be evaluated from (14) for a periodic crystal where the convolution integrals become summations over reciprocal lattice points and the final Fourier transform to obtain the intensity distribution is trivial.

If $\Psi(\mathbf{u})$ is small in magnitude except for a large peak at the origin, then (14) can be easily interpreted. In this case the exponential term in (14*a*) can be neglected, since for the strong terms either $\mathbf{u}'=0$ or $\mathbf{u}'-\mathbf{u}=0$, and

$$\mathscr{I}(\mathbf{u})={}^{\Delta}\Psi(\mathbf{u})*{}^{\Delta}\Psi\ (-\mathbf{u}) \tag{16}$$

so that

$$I(\mathbf{r})=|{}^{\Delta}\psi(\mathbf{r})|^2 \tag{17}$$

where ${}^{\Delta}\psi(\mathbf{r})=\mathscr{F}{}^{\Delta}\Psi(\mathbf{u})$. In this case, the effect of chromatic aberration is simply to attenuate the diffraction pattern amplitudes by the function $\exp(-\frac{1}{2}\pi^2\lambda^2\Delta^2u^4)$. This is equivalent to introducing a fuzzy aperture into the back-focal plane of the objective lens. Thus the inclusion of chromatic aberration in the image calculations can produce an effect similar to that of decreasing the size of the aperture which was found necessary in order to make the calculations agree with experiment.

If it is assumed that the spatial frequencies are effectively cut off owing to chromatic aberration when they are attenuated to one tenth of their original amplitude by the attenuating factor in (14*b*), then the highest spatial frequency contributing to the image is given by

$$u_{\max}\simeq 0{\cdot}83\lambda^{-1/2}\Delta^{-1/2}. \tag{18}$$

Therefore to given an effective aperture radius of 0·263 Å^{-1} as was used in the calculations for Fig. 2(*b*), $\Delta=250$ Å. Using the reciprocal of this maximum spatial frequency as a limit to the best attainable resolution, one obtains the chromatic aberration limit to resolution as

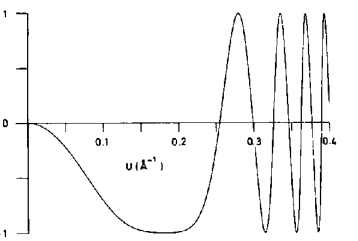

Fig. 3. Radial part of sin $\chi(\mathbf{u})$ with $\varepsilon=-800$ Å, $C_s=1{\cdot}8$ mm.

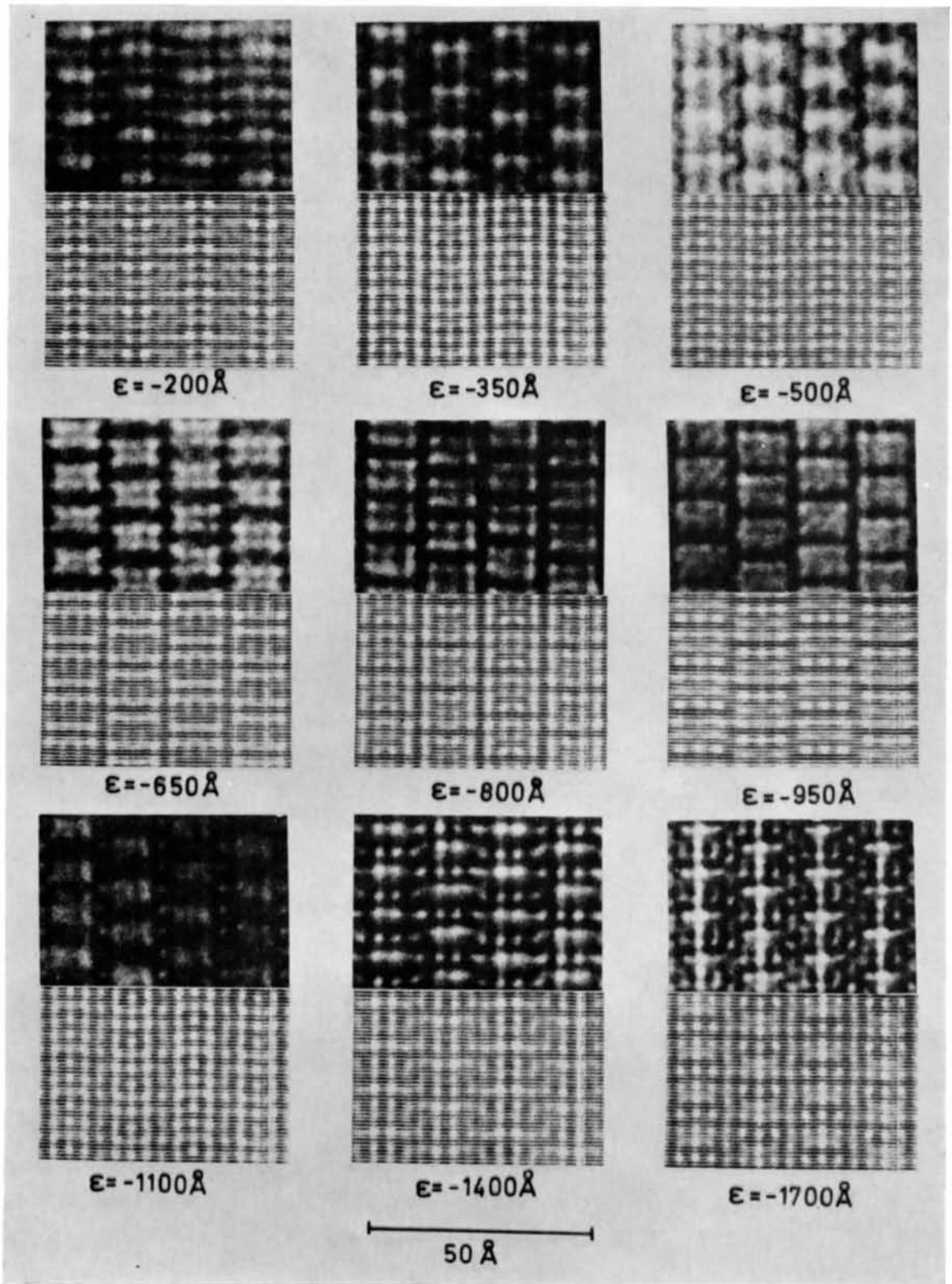

(*a*)

Fig. 2. (*a*) Through-focus series of images from $Ti_2Nb_{10}O_{29}$. The amount of defocus (ε) is indicated below each image. In each case, the top image is the experimental one (taken by S. Iijima) while the bottom image is the calculated one using the following parameters: $C_s = 1.8$ mm, objective-aperture radius is 0.33 Å^{-1} and no chromatic aberration is assumed.

[*To face p.* 112

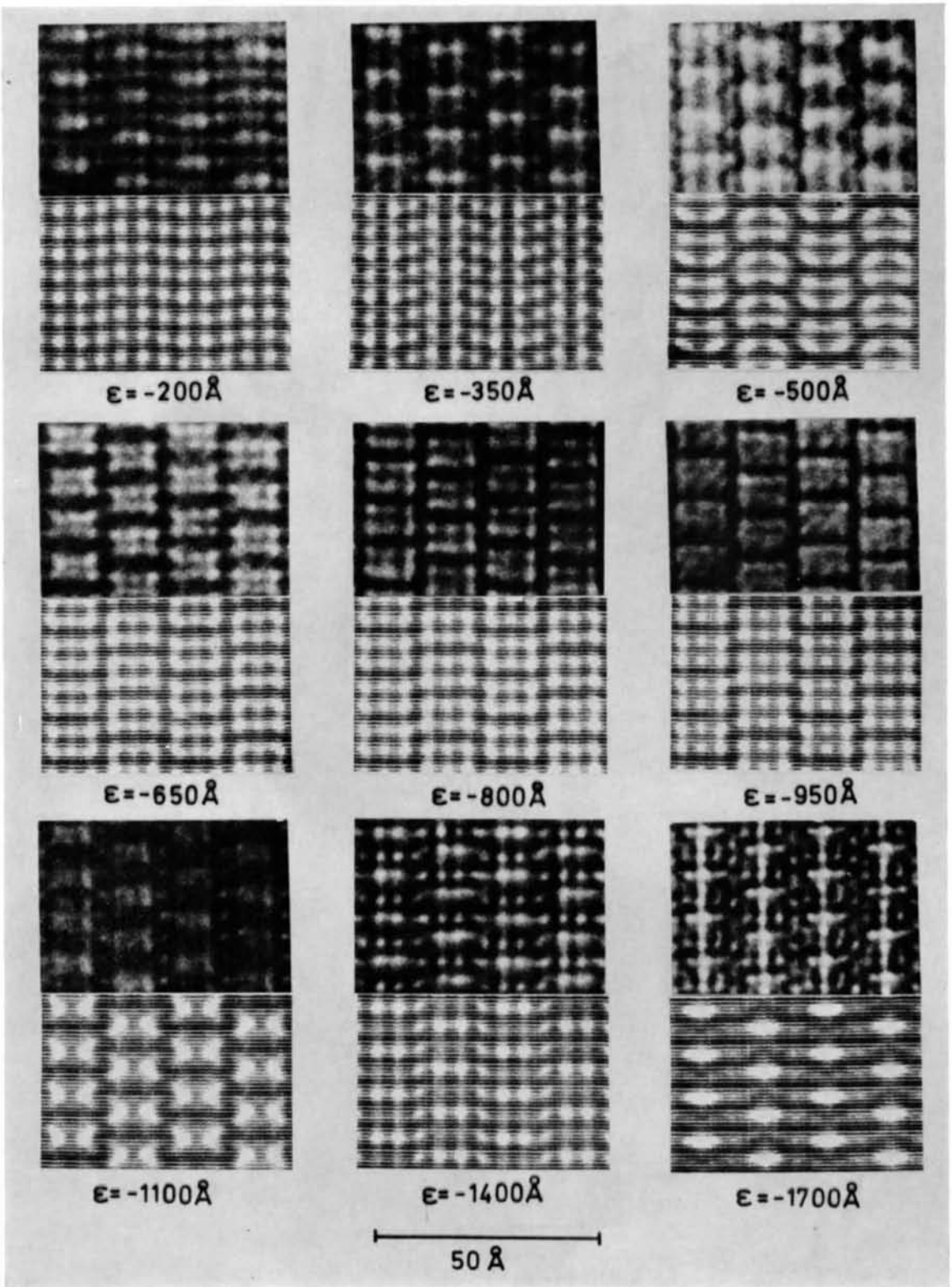

(*b*)

Fig. 2. (*b*) $C_s = 1.8$ mm, objective-aperture radius is 0.263 Å^{-1} and no chromatic aberration is assumed.

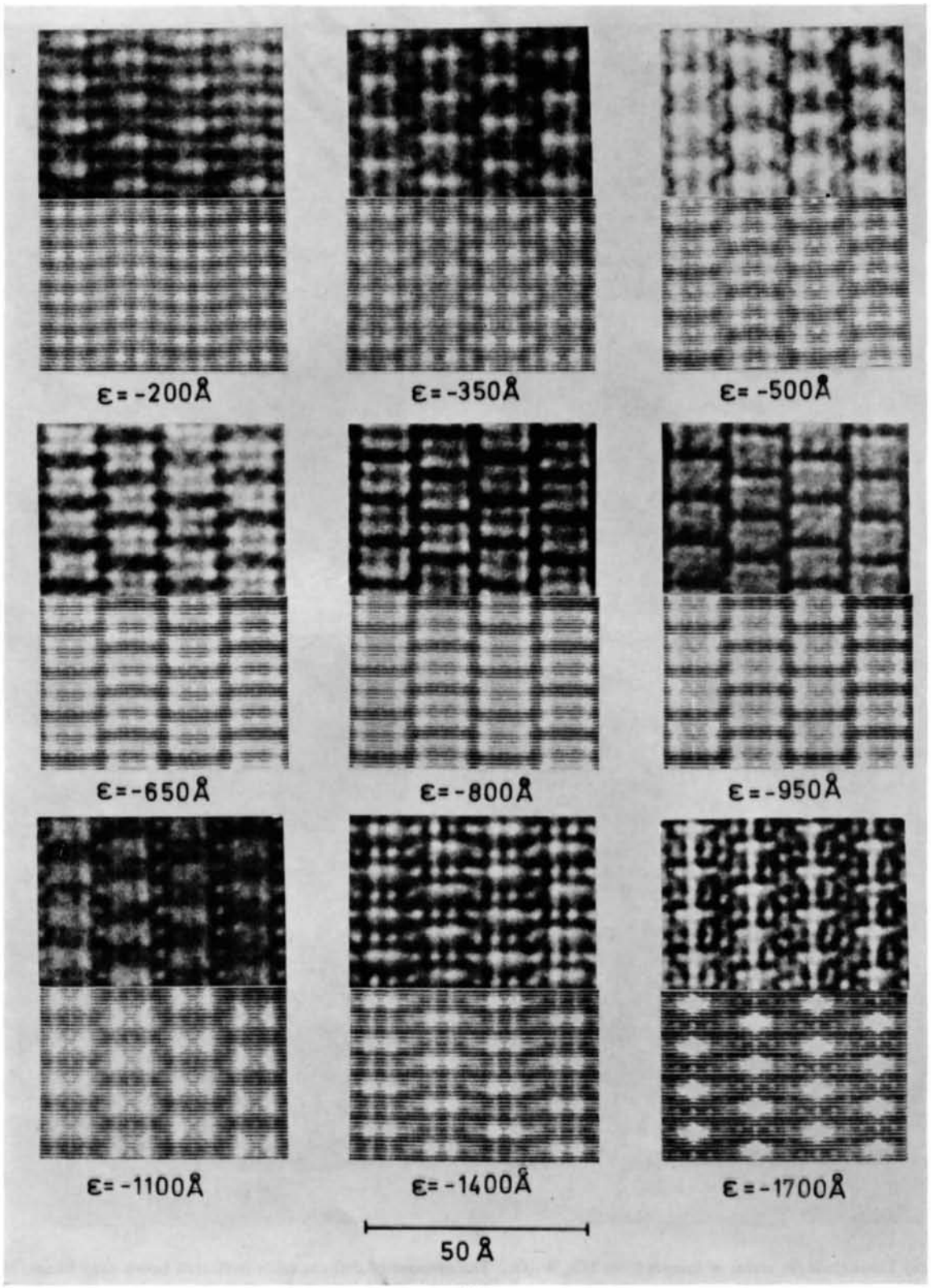

(*c*)

Fig. 2. (*c*) $C_s = 1.8$ mm, objective-aperture radius is 0.33 Å^{-1} and the spread of defocus (Δ) due to chromatic aberration is 250 Å.

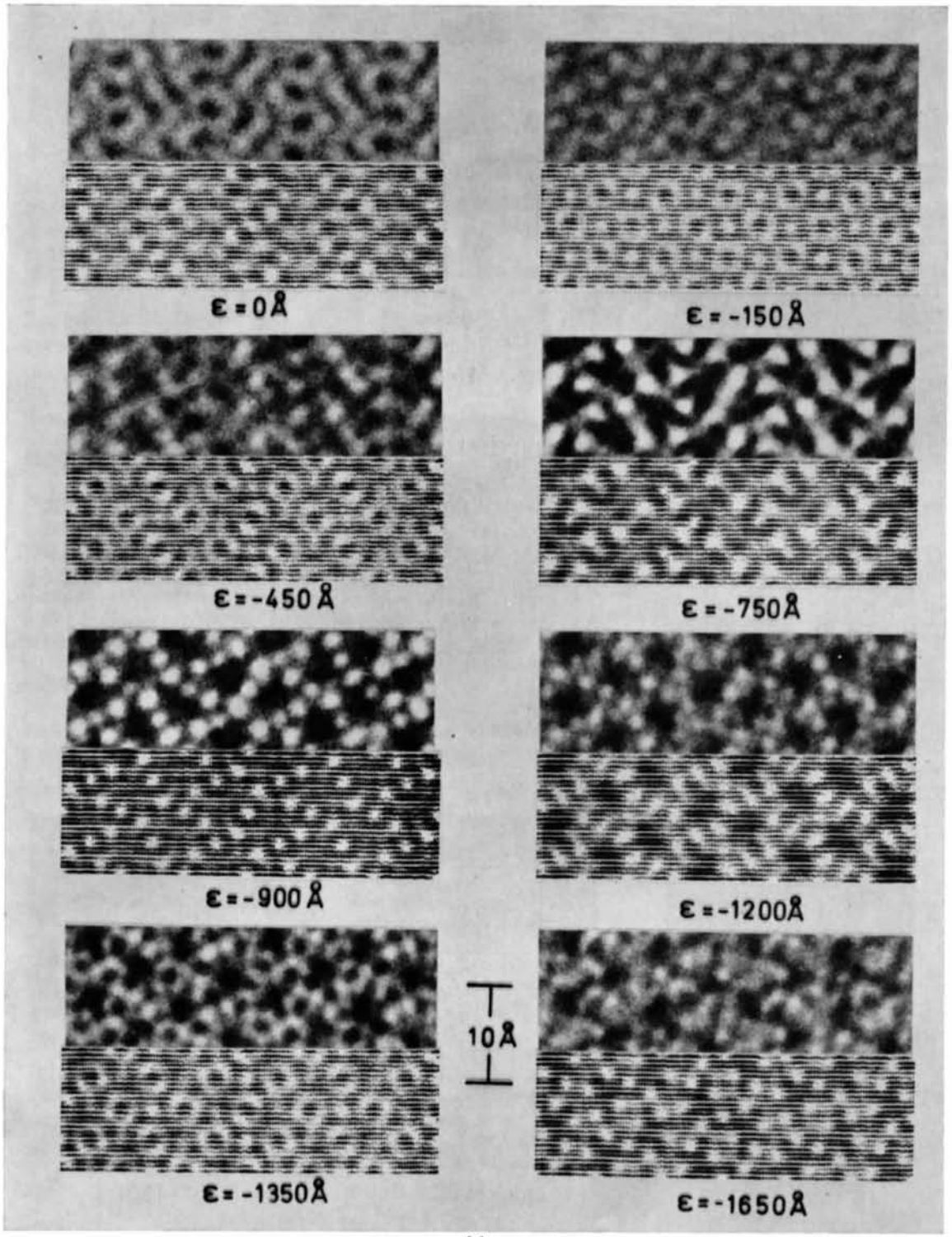

(*a*)

Fig. 4. (*a*) Through-focus series of images from $Nb_{16}W_{18}O_{94}$. The amount of defocus (ε) is indicated below each image. In each case, the top image is the experimental one (taken by S. Iijima) while the bottom image is the calculated one using the following parameters: $C_s = 1.8$ mm, objective-aperture radius is 0·263 Å^{-1} and no chromatic aberration is assumed.

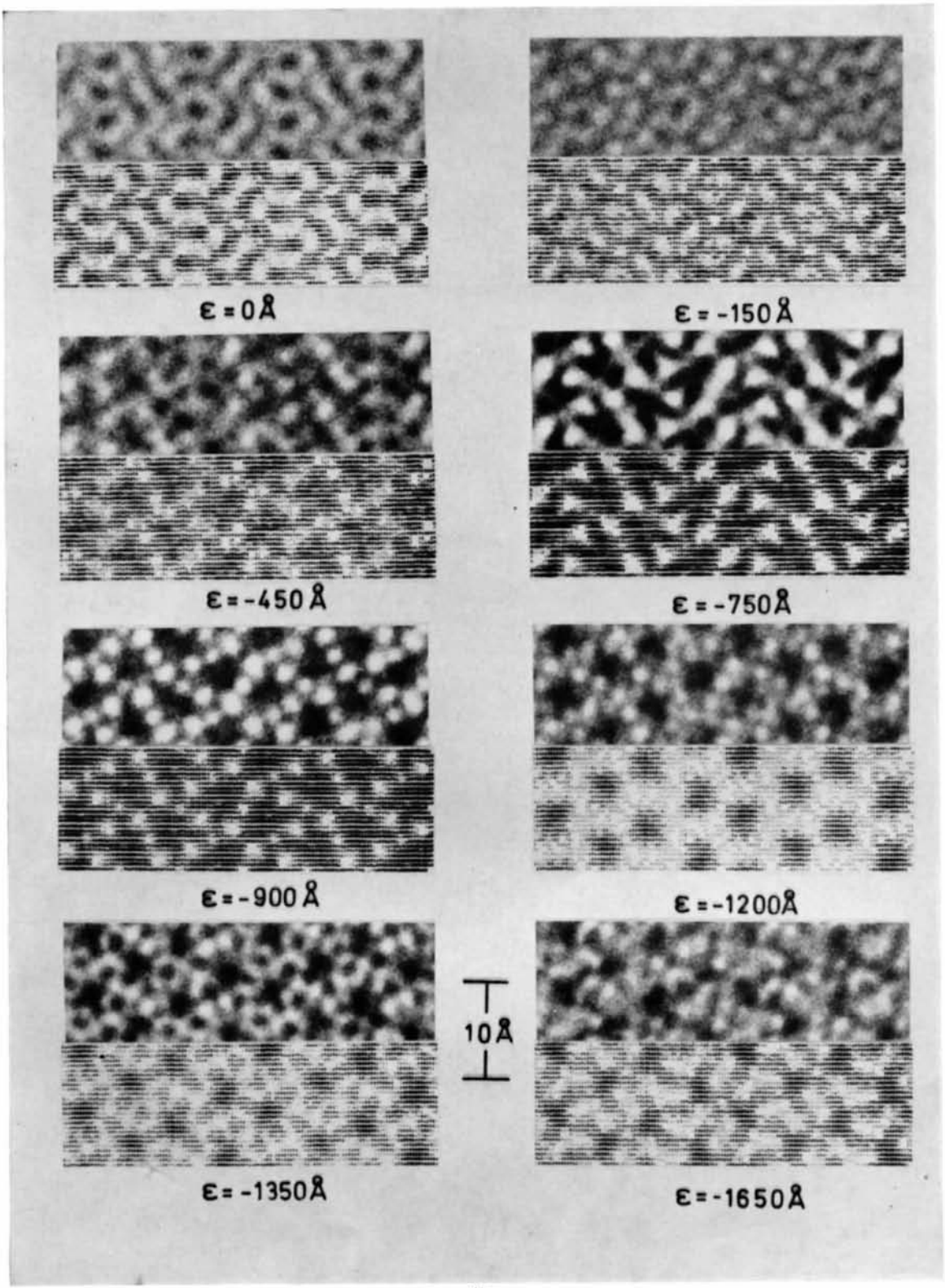

(*b*)

Fig. 4. (*b*) $C_s = 1.8$ mm, objective-aperture radius is 0·33 Å^{-1} and the spread of defocus (Δ) due to chromatic aberration is 250 Å^{-1}.

$$d \simeq 1{\cdot}2\sqrt{\lambda\Delta} \simeq 0{\cdot}23\sqrt{\Delta} \qquad (19)$$

for 100 keV electrons.

Fig. 2(*c*) shows a through-focus series of images calculated including chromatic aberration with $\Delta =$ 250 Å. A spherical aberration constant of 1·8 mm and an objective aperture radius of 0·33 $Å^{-1}$ were assumed. The calculated images for the whole through-focus series are now in very good agreement with the experimental images.

Calculations were also carried out for $Nb_{16}W_{18}O_{94}$ assuming a structure determined by Sleight (1966). Fig. 4(*a*) and (*b*) shows a comparison between experimental images obtained by Iijima and calculated images for a through-focus series. The calculations for Fig. 4(*a*) do not include chromatic aberration and assume an objective aperture radius of 0·263 $Å^{-1}$. Fig. 4(*b*) shows the results when chromatic aberration is included with $\Delta = 250$ Å and the objective aperture radius is increased to 0·33 $Å^{-1}$. Here again the calculated images agree very well with experiment when chromatic aberration is included in the calculations.

Discussion

The calculated images shown above indicate that it is possible to obtain good agreement with experiment when chromatic aberration is taken into account. The calculations assumed a spread of defocus of 250 Å which corresponds to an energy spread of $\sim 1{\cdot}5$ eV in the electrons. This is larger than the expected thermal energy spread from the source and even when part of this spread is attributed to instabilities, this value is larger than expected. One possible explanation of this is found in the calculations of O'Keefe & Sanders (1975) which show that the effect of divergence of the incident beam will be to reduce the resolution in the image in much the same way as the effect of chromatic aberration discussed above. In this case, the image needs to be averaged incoherently over the cone of illumination. O'Keefe & Sanders did this by calculating image intensities for various incident beam directions in the cone and then averaging.

However, an indication of the effect of beam divergence can be obtained by performing this averaging analytically over the intensity in a similar way to which chromatic aberration was treated. Then, if it is again assumed that most of the diffraction-pattern intensity is in a peak at the origin, it can be shown that the diffraction pattern amplitudes are modulated by a function $2J_1[2\pi\alpha(\varepsilon u + C_s\lambda^2 u^3)]/2\pi\alpha(\varepsilon u + C_s\lambda^2 u^3)$, where α is the half angle of the cone of divergence and J_1 is a Bessel function of the first order. The effect of different crystal projections has been neglected and so this is only valid for thin crystals. This is very similar to the effect of chromatic aberration derived above and so if beam divergence is neglected in the calculations, an excessive amount of chromatic aberration can compensate for it. It is therefore expected that if the images shown above were to be recalculated assuming the correct amount of beam divergence and only a small spread of defocus, then they would not be appreciably altered.

The calculations shown here have all been done for very thin crystals, using a phase-grating approximation. They show good agreement with experiment, but for thicker crystals complete *n*-beam calculations, such as multislice calculations as have been done by O'Keefe & Sanders (1975) and Goodman & Moodie (1974), are necessary. In addition, these calculations have only been done for a particular type of crystal structure and under a limited range of conditions so that the results cannot automatically be assumed to apply to general imaging problems until a wider variety of detailed calculations have been done. However, this work does indicate the importance of correctly including the microscope aberrations, such as chromatic aberration, when calculating high-resolution images and gives a method by which this may be done.

The author is greatly indebted to Professor J. M. Cowley for his help and encouragement during the course of this work and he wishes to thank Dr Sumio Iijima for providing the electron micrographs and for permission to use these.

This work was supported by the National Science Foundation Area Development Grant in Solid State Science, No. GU-3169.

References

ALLPRESS, J. G. & SANDERS, J. V. (1973). *J. Appl. Cryst.* **6**, 165–190.

BUSECK, P. R. & IIJIMA, S. (1974). *Amer. Min.* **59**, 1–21.

COWLEY, J. M. & IIJIMA, S. (1972). *Z. Naturforsch.* **27a**, 445–451.

COWLEY, J. M. & IIJIMA, S. (1976). In *Electron Microscopy in Mineralogy*, edited by H. R. WENK & G. THOMAS. Berlin: Springer-Verlag.

COWLEY, J. M. & MOODIE, A. F. (1960). *Proc. Phys. Soc.* **76**, 378–384.

FEJES, P. L. (1972). *30th Ann. Proc. Electron Microsc. Soc. Amer. Los Angeles, Calif.* 1972, edited by C. J. ARCENEAUX, pp. 558–559.

GOODMAN, P. & MOODIE, A. F. (1974). *Acta Cryst.* A**30**, 280–290.

LYNCH, D. F., MOODIE, A. F. & O'KEEFE, M. A. (1975). *Acta Cryst.* A**31**, 300–307.

O'KEEFE, M. A. & SANDERS, J. V. (1975). *Acta Cryst.* A**31**, 307–310.

SLEIGHT, A. W. (1966). *Acta Chem. Scand.* **20**, 1102–1112.

WADSLEY, A. D. (1961). *Acta Cryst.* **14**, 664–670.